Talanta 123 (2014) 101–108

Contents lists available at ScienceDirect

Talanta

journal homepage: www.elsevier.com/locate/talanta

Fe_3O_4@rGO doped molecularly imprinted polymer membrane based on magnetic field directed self-assembly for the determination of amaranth

Qing Han, Xi Wang, Zaiyue Yang, Wanying Zhu, Xuemin Zhou*, Huijun Jiang*

School of Pharmacy, Nanjing Medical University, Nanjing 211166, PR China

ARTICLE INFO

Article history:
Received 21 November 2013
Received in revised form
24 January 2014
Accepted 25 January 2014
Available online 6 February 2014

Keywords:
Fe_3O_4@rGO
Directed self-assembly
Molecularly imprinted polymer
Electrochemical sensor
Amaranth

ABSTRACT

Based on magnetic field directed self-assembly (MDSA) of Fe_3O_4@rGO composites, a novel magnetic molecularly imprinted electrochemical sensor (MIES) was fabricated and developed for the determination of the azo dye amaranth. Fe_3O_4@rGO composites were obtained by a one-step approach involving the initial intercalating of iron ions between the graphene oxide layers via the electrostatic interaction, followed by the reduction with hydrazine hydrate to deposit Fe_3O_4 nanoparticles onto the reduced oxide graphene nanosheets. In molecular imprinting, the complex including the function monomer of aniline, the template of amaranth and Fe_3O_4@rGO was pre-assembled through π–π stacking and hydrogen bonding interactions, and then was self-assembled on the surface of magnetic glassy carbon electrode (MGCE) with the help of magnetic field induction before electropolymerization. The structures and morphologies of Fe_3O_4@rGO and the doped molecularly imprinted polymers (MIPs) were investigated by Fourier transform infrared spectrometer (FT-IR), Raman spectra and scanning electron microscope (SEM). Besides, the characterization by differential pulse voltammetry (DPV) showed that Fe_3O_4@rGO composites promoted the electrical conductivity of the imprinted sensors when doped into the MIPs. The adsorption isotherms and adsorption kinetics were employed to evaluate the performances of MIES. The detection of amaranth was achieved via the redox probe $K_3[Fe(CN)_6]$ by blocking the imprinted cavities, which avoided the interferences of oxidation products and analogs of amaranth. Furthermore, the prepared MIES exhibited good sensitivity, selectivity, reproducibility and efficiency for detecting amaranth in fruit drinks. The average recoveries were 93.15–100.81% with the RSD $< 3.0\%$.

1. Introduction

The modification of electrode surfaces has constituted a very active research field for decades due to the strong interest in designing electrochemical sensors and biosensors based on electrocatalysis for chemical analysis and biological detection. The novel strategies and materials for fabricating the modified electrode were explored extensively in improving the performance and potential practical uses which required good catalytic activity for target molecules or probe molecules, fast electron transfer kinetics, low diffusion limitation, high stability and reproducibility [1–4].

Many approaches have been employed to construct these modified electrodes, such as spin-coating [5], casting [6,7], self-assembly [8–11], covalent cross-linking [12], and electro-deposition [13,14]. Among the possible methods, self-assembly has attracted attention of so many researchers in the field of nanotechnologies and nanomaterials [15–18]. Although general self-assembly, particularly layer-by-layer self-assembly (LBL), was an efficient way for the fabrication of modified electrode [19–22] by means of hydrogen bonding, electrostatic attraction, π–π stacking, donor–acceptors, van der Waals, hydrophilic and hydrophobic interactions. However, the preparation of modified electrode by LBL was usually time-consuming and resource-wasting because sufficient solvent was needed for removing the unbound nanomaterials in the process of alternating assembly [23].

Directed self-assembly (DSA) used the basic principles of self-assembly by carefully choosing and constructing the building blocks, and promoted the process by modulating the thermodynamic forces without going into advanced and complicated technique. There were two broad divisions containing template-guided self-assemblies (e.g. physical template, chemical template and biological template) and field-guided self-assemblies

* Corresponding authors. Tel./fax: +86 25 86868476.
E-mail addresses: xueminzhou001_001@hotmail.com (X. Zhou), huijun_jiang2006@hotmail.com (H. Jiang).

http://dx.doi.org/10.1016/j.talanta.2014.01.060
0039-9140

(e.g. magnetic field, electric field, pressure gradient, light and laser) among DSAs [9,18]. Magnetic field directed self-assembly (MDSA), a recently emerged external self-assembled approach [24,25], has shown an excellent prospect for the fabrication of modified electrodes [26–28]. In these systems, magnetic field could rapidly drive and conveniently orient magnetic nanoparticles, controlling the final three-dimensional architectures in the preparing process of electrode modification.

Recently, magnetite (Fe_3O_4), one promising magnetic nanoparticle, has been widely utilized in various fields, such as targeted drug delivery and sensors, especially in electrochemistry due to their distinguished magnetic and electrochemical properties. However, Fe_3O_4 nanoparticles were not only easy to be oxidized in air, but also tended to highly aggregate in aqueous systems, which in turn hindered the electron transfer [29,30]. To overcome these obstacles, many nanostructured materials containing carbons, metals, and conducting polymers have been developed to hybridize with Fe_3O_4 nanoparticles [31–33].

Graphene, a two-dimensional nanomaterial with one or several atomic layers of carbons, has become an ideal material for the preparation of sensors owing to its novel properties such as large specific surface area, exceptional thermal and mechanical properties, and high electrical conductivity [34–36]. Therefore, it could be a satisfactory matrix for preparing the magnetic composites by intercalating Fe_3O_4 nanoparticles onto the lamellar structure of the reduced oxide graphene, which avoided the aggregation and oxidation of Fe_3O_4. Furthermore, due to the special magnetism and excellent electrical conductivity, reduced oxide graphene-based composite materials with Fe_3O_4 were highly desirable for rapidly assembling functionalized sensing interfaces as well as accelerating electron transfer and improving the catalytic activity in electrochemical and biological sensors [37,38].

In our recent studies, we have exploited different strategies for the modification of electrodes before preparing molecularly imprinted polymers (MIPs) containing "sandwich"-casting and LBL assembly, and found that nanostructured reduced oxide graphene could dramatically increase the intensity of the electrochemical signal, facilitating the development of MIES in ultrasensitive assays [39,40]. Further research on MIPs was developed via integrating functionalized Au nanoparticles (F-AuNPs) into imprinted sensing membrane. The doping F-AuNPs were used as electroactive and conductive labels to improve the sensitivity, and simultaneously employed as "carriers" to deliver analyte more easily to the electrode surfaces [41]. Doping reduced oxide graphene-based composites with Fe_3O_4 into the three dimensional structure of MIPs could be another attempt which might have the advantages of rapid assembly and easy immobilization besides promoting the electrical conductivity.

Amaranth, a typical synthetic aromatic azo dye, was used extensively to give fascinating red color to drinks, sirups, and sweets. However, studies have shown that amaranth could cause many adverse health effects such as high genotoxicity, cytostaticity and cytotoxicity [42,43]. Although electrochemical methods have been successfully developed for the detection of amaranth, the hard removal of oxidized products on the surface of modified electrode as well as the interference of analogs limited the applied scope of some sensors.

In this article, a novel MIES for the detection of amaranth was fabricated by magnetic field induced self-assembly of reduced oxide graphene-based composites with Fe_3O_4 (Fe_3O_4@rGO). The doped imprinted membrane was constructed via the electropolymerization with the assistance of MDSA in the pre-assemble solution containing amaranth, aniline and Fe_3O_4@rGO. The thickness and morphologies of the doped MIPs could be easily controlled by adjusting the concentration of Fe_3O_4@rGO composites. Spectral and electrochemical approaches were employed in the characterization of Fe_3O_4@rGO composites and the doped imprinted membrane. Also, the fabricated MIES was used to detect the amaranth in fruit drinks, and revealed a high sensitivity and excellent selectivity.

2. Experimental

2.1. Reagents and apparatus

Amaranth (analysis of standard), allure red, new coccine, erythrosine were purchased from Aladdin reagent (Shanghai, China); Graphite powder (99.9995%, 325 mesh) was purchased from Alfa Aesar (Britain); aniline was obtained from Ling feng chemical reagent Co., Ltd. (Shanghai, China). Hydrazine hydrate, Shanghai Experiment Reagent Co., Ltd., China; H_2SO_4 was purchased from Shanghai chemical reagent Co., Ltd. (China). The acetate buffer solution (ABS) was prepared by mixing the stock solution of NaAc and HAc. The phosphate buffer solution (PBS) was prepared by mixing the stock solution of Na_2HPO_4 and NaH_2PO_4. All other chemicals were of analytical grade and used without further purification. The electrolyte solution was prepared by double distilled water and purged with nitrogen for 10 min before using.

Electrochemical data were obtained with a three-electrode system using an electrochemical analyzer (CHI 660D, China). MGCE (Φ=3 mm, magnetic flux density=1.600 T) was purchased from Tianjin Incole Union Technology Co., Ltd. (Tianjin, China). Scanning electron microscope (SEM) images were recorded with S-4800 and S-3400N (Hitachi, Japan). Raman spectra were performed by using a DXR Smart Raman Spectrometer excited with 633 nm laser radiation (Thermo Scientific, USA).

2.2. Synthesis of Fe_3O_4@rGO

Graphene oxide (GO) was first synthesized by a modified Hummers method and then Fe_3O_4@rGO composites were prepared according to the literature reported [44]. Briefly, 4.0 mL 6.5 mg mL^{-1} GO was dispersed in 35 mL deionized water by ultrasonic for 1 h. Then, 4.0 mL 0.2 mmol mL^{-1} $FeCl_3 \cdot 6H_2O$ and 0.1 mmol mL^{-1} $FeCl_2 \cdot 4H_2O$ were added dropwise to GO solution at room temperature under nitrogen flow with vigorous stirring for 1 h. After that, 28% ammonia solution was added drop by drop to make solution pH 10 for synthesis of Fe_3O_4 nanoparticles, the temperature of the solution rose to 80 °C and 0.2 mL hydrazine hydrate was added with continuously stirring for the reduction of GO. After being rapidly stirred for 10 h, the solution was cooled down to room temperature. The obtained black Fe_3O_4@rGO composites were separated by external magnetic field and washed with deionized water to pH=7, then stored in 50 mL nitrogen saturation deionized water at 4 °C. The synthesized Fe_3O_4@rGO composites had good adsorption property to amaranth by π–π stacking interactions and hydrogen bonding, which are shown in Fig. S1.

2.3. Preparation of MIES

5 mL mixed ABS (pH 6.0) containing 0.5 mg mL^{-1} Fe_3O_4@rGO, 150 mmol L^{-1} H_2SO_4 and 3.0 mmol L^{-1} amaranth were placed in dark at room temperature for 4 h with moderately stirring under nitrogen to complete the pre-assembly through π–π stacking interactions and hydrogen bonding. Then, 27.6 μL aniline was added into the mixed solution with stirring and nitrogen in dark for another 1 h. Afterwards, the magnetic glassy carbon electrode (MGCE) was inserted into the pre-assembled complex solution for 10 min, and the MIES was prepared by constant potential polymerization at 1.0 V for 700 s. Finally, in the washing procedure, the imprinted electrode was immersed into 5.0 mL 0.5 mol L^{-1} H_2SO_4 solution and treated with a constant potential at −0.6 V for 200 s

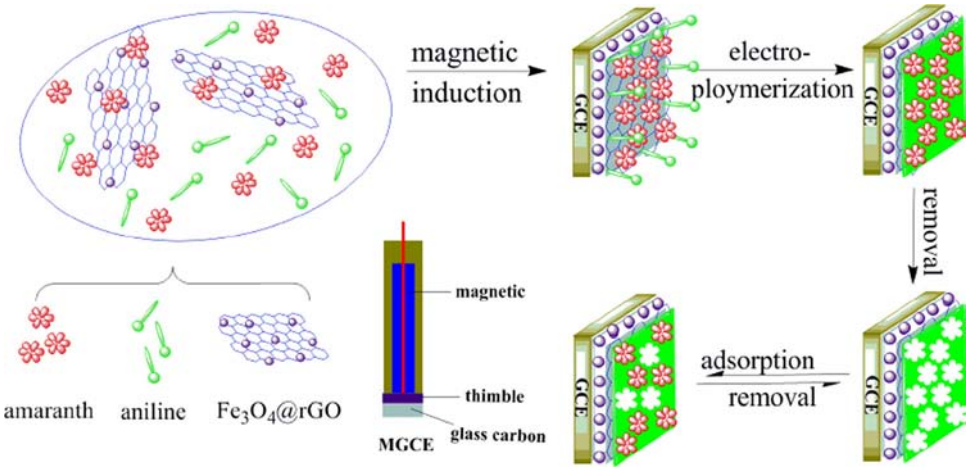

Scheme 1. Schematic representation for the preparation of MIES.

to remove targeted molecules, and dried under nitrogen. The route for fabrication of MIES is shown in Scheme 1. Non-molecular imprinted electrochemical sensor (NIES) was prepared except for the addition of template molecules in pre-assembling solution.

2.4. Experimental measurements

Electrochemical measurements were carried out in a 10.0 mL aqueous solution containing 1 mmol L^{-1} of $K_3[Fe(CN)_6]$ and 0.1 mol L^{-1} of KCl. In differential pulse voltammetry (DPV) measurements, the scan was performed from −0.1 V to 0.4 V, pulse width, pulse period and quiet time were 0.02 s, 0.1 s and 2 s, respectively.

Film-forming factors (the amount of Fe_3O_4@rGO and amaranth, dosage of aniline, polymerization time and elution time) were optimized by comparing the changed oxidation value of peak current of redox probe $K_3[Fe(CN)_6]$ ($\Delta I_p = I_2 - I_1$, the current value of MIES after electropolymerization was I_1 and the current value of MIES after removing templates was I_2.). The current change before and after the electrochemical polymerization could reflect imprinting effect of the MIES. The greater the peak current value changed, the more the targeted imprinted sites were. On the other hand, the adsorption performances of MIES were investigated by calculating the changes of the current value between before and after adsorption ($\Delta I_p = I_3 - I_4$, the current value of MIES before and after adsorption target molecules was I_3 and I_4, respectively.). When amaranth molecules were adsorbed, they occupied the specific imprinted sites, and reduced the current signal by hindering the probe to contact with the electrode surface.

3. Results and discussion

3.1. Characterization

Fig. 1A depicts FTIR spectra of GO and Fe_3O_4@rGO. In GO spectrum (Fig. 1A.a), several characteristic peaks could be observed, C=O (1725 cm^{-1}), alkoxy C–O (1393 cm^{-1}, 1237 cm^{-1}, and 1066 cm^{-1}) stretching vibrations were observed. In Fig. 1A.b, the absorption band at 1725 cm^{-1} almost disappeared, indicating C=O was reduced. The peaks at 1593 cm^{-1} of GO and Fe_3O_4@rGO could be attributed to the skeletal vibration of the graphene sheets [45,46]. The characteristic absorption corresponding to the stretching vibration of Fe–O bond was shifted to higher wavenumber of 638 cm^{-1} compared to that of 570 cm^{-1} reported for the stretching

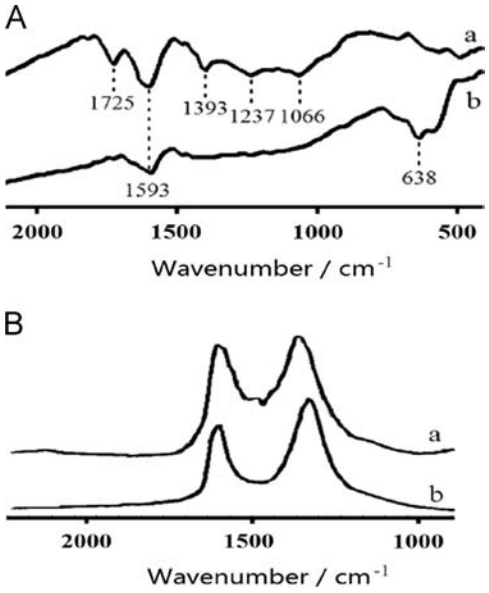

Fig. 1. (A) FTIR of GO (a) and Fe_3O_4@rGO (b), (B) Raman spectra of GO (a) and Fe_3O_4@rGO (b).

mode of Fe–O in bulk Fe_3O_4, suggesting that Fe_3O_4 was bound to the surface of graphene sheets [47].

Fig. 1B shows Raman spectra of GO and Fe_3O_4@rGO. GO spectra displayed two prominent peaks: G-band at around 1600 cm^{-1} corresponding to a well defined sp^2 carbon-type structure, and D-band at around 1360 cm^{-1} attributing to defects within the hexagonal graphitic structure. Thus a smaller I_D/I_G intensity ratio of Raman spectrum indicated lower defects and disorders of the graphitized structures. The I_D/I_G of hybridized products Fe_3O_4@rGO increased from 1.04 for GO to 1.33, suggesting that there were more defects in reduced oxide graphene after treatment. Similar phenomenon had been interpreted in elsewhere [48] with the assumption that the reduced state increased the number of aromatic domains of smaller size, leading to an increase of the I_D/I_G intensity ratio. Therefore, we could deduce that GO has been well deoxygenated during the addition of hydrazine hydrate from the Raman spectrum.

To investigate the morphologies and structures of the products, SEM images were taken for the obtained Fe_3O_4@rGO. Fig. 2A and B presents the SEM images of Fe_3O_4@rGO, the lamellar structure of graphene decorated by a large number of spherical Fe_3O_4 nanoparticles could be clearly observed.

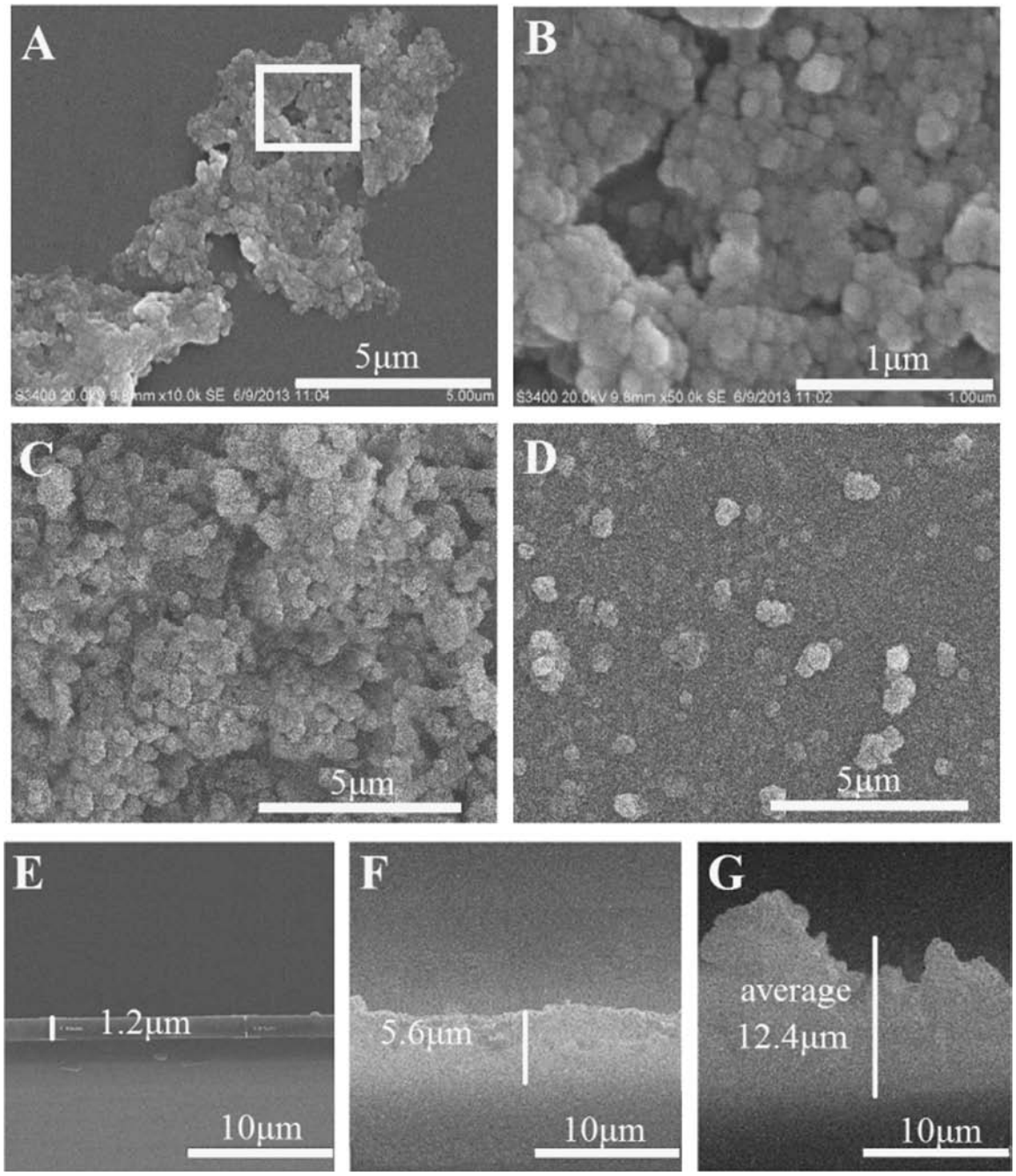

Fig. 2. Morphologies characterization of SEM. (A and B) Fe_3O_4@rGO, B was the local magnification effect of A. (C) MMIP, (D) NMIP, (E–G) section thickness of MIPs with different concentration, the complex concentration in F was used for the preparation of MIES. The complex concentration in E was half of that in F, while the concentration in G was 1.5 times of that in F.

The morphologies of MIP membrane based on MDSA (MMIP) and the MIP membrane without magnetic field induction (NMIP) were characterized by SEM. The iron element was detected in MMIP (Fig. S2A), revealing Fe_3O_4@rGO composites were successfully doped into MIPs based on MDSA. On the contrary, the iron element was not detected in NMIP (Fig. S2B). DPV was used to study the differences between MMIP and NMIP, and the results are shown in Table S1.

Appropriate thickness of the nanostructure layer could accelerate the electrical conductivity and increase the amount of effective imprinted sites, resulting in improving the sensitivity of MIES. Fig. 2E–G shows the section thickness of MIPs with different concentration under fixed proportion of amaranth, Fe_3O_4@rGO and aniline in pre-assembling solution. The complex concentration in F was used for the preparation of MIES. The complex concentration in E was half of that in F, while the concentration in G was 1.5 times of that in F. The average thickness of E–G was about 1.2 μm, 5.6 μm and 12.4 μm, respectively. The MIP in E was thin, which would result in the poor electrical conductivity and perhaps influenced the imprinting effects. Although the MIP in G possessed good performance of electrons conduction, its shape was uneven which indicated the probable faster aggregation of magnetic composites in the process of pre-assembling and magnetic field induction. The favorable electrical conductivity and more uniform morphology both belonged to the MIP in F, which revealed the selected concentration of pre-assembling solution was suitable.

3.2. Electrochemical behavior of MIES

DPV was used to characterize the imprinted sensor. Fig. 3 shows the DPVs of different surface conditions on one electrode. It was found that the oxide peak current increased after electropolymerization onto the surface of bare MGCE, which might owe to the excellent electrical conductivity of Fe_3O_4@rGO composites, enhancing the electrons transfer rate. The oxidation peak value obviously increased after templates removal, the possible reason was that the recognition cavities were exposed after templates removal and the probe molecules $K_3[Fe(CN)_6]$ could reach the surface of the sensor without obstacle.

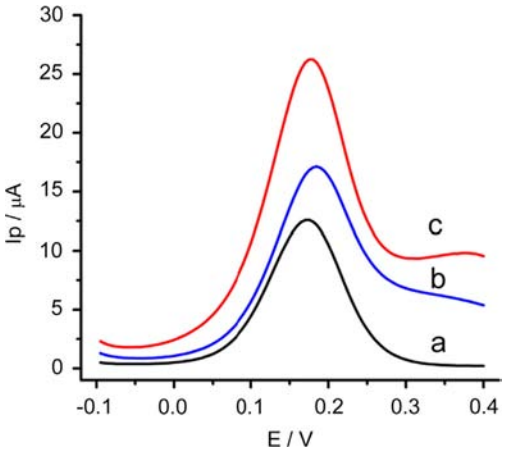

Fig. 3. Typical DPV study of $[Fe(CN)_6]^{3-/4-}$ at (a) a bare MGCE, (b) after electropolymerization, and (c) after remove of amaranth molecules.

3.3. Condition optimization of MIES for amaranth

In pre-assembling process, Fe_3O_4@rGO interacted with template molecules through π–π stacking interactions, moreover, Fe_3O_4@rGO also acted as modified nanomaterials doped into MIP to improve electrons transfer of probe molecules. Therefore, the optimization of the suitable amounts of Fe_3O_4@rGO and amaranth was a crucial factor for the study of MIES. The amounts of Fe_3O_4@rGO and amaranth were optimized at five mass concentration ratios when the amount of aniline remained unchanged. In Fig. 4A, the MIES with the ratio of 3.5:1 had a highest changed value of peak current in probe solution, indicating the MIES had a better imprinting effect.

Aniline acted as functional monomer to interact with amaranth via hydrogen bonding, and also used as cross-linker for forming three-dimensional imprinted membrane layer in the electrochemical polymerization process. The amount of aniline directly impacted on the number of the imprinted cavities. Low amount of aniline leaded to be difficult to produce effective imprinted cavities. However, superabundant aniline would result in excessive cross-linking, templates embedded too deep to remove. Fig. 4B indicates that the best amount of aniline was 60 mmol L^{-1}.

The scan time during the electrochemical polymerization process could control the thickness of the doped MIPs membrane, which was closely related to imprinting effect. The imprinted layer was a green conductive film. When scan time was shorter than 400 s, the electro-conductivity of the film was poor. As extending

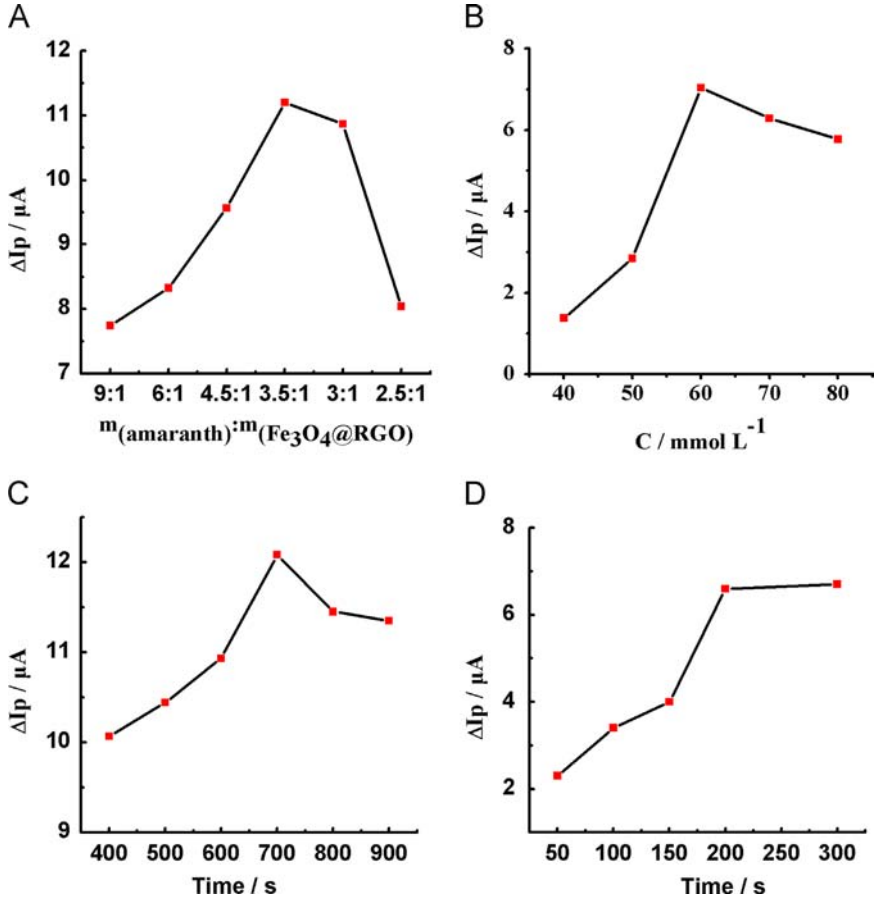

Fig. 4. (A) Optimization of the mass concentration ratios between Fe_3O_4@rGO and amaranth molecules, (B) optimizing the amount of aniline, the effects of (C) electropolymerization time and (D) electro-elution time.

the scan time, the ΔI_p increased and the color of green film deepened, indicating the augment of film's thickness. When scan time was more than 700 s, ΔI_p reduced, demonstrating the decrease of effective imprinted cavities. Fig. 4C shows the optimal scan time for electropolymerization was 700 s.

The elution of template molecules was a key step to obtain specific imprinted cavities. In the experiment, we used the electro-elution under acidic conditions and achieved good results. Amaranth could be eluted by immersed in H_2SO_4 for a long time; while under electro-elution, elution time shortened greatly. Fig. 4D demonstrates the relationship between elution time and imprinting effect. When time was shorter than 200 s, templates could not be removed fully. When time was longer than 200 s, current value of peak almost no longer changed, therefore 200 s was chosen as the final elution time.

3.4. Evaluation of the adsorption characteristics of MIES

The adsorption isotherms of MIES and NIES to amaranth are plotted in Fig. 5A. The adsorption of amaranth could cause current value dropping. For MIES, ΔI_p added with the increasing of the concentration of templates until it reached equilibrium and the response of NIES almost did not change. It exhibited the MIES had a better memory function and a higher adsorption capacity for amaranth and NIES had little adsorption.

The adsorption kinetics of MIES was investigated with amaranth solution at different time intervals. As shown in Fig. 5B, MIES had fast adsorption kinetics within approximately 25 min. Even if the initial concentrations of amaranth were different, the saturation adsorption capacities were almost the same. This indicated that the number of effective imprinted cavities in the doped membrane was almost constant.

The selectivity property of MIES was investigated with 100-fold concentration ratio of other three artificial colors erythrosine, new coccine and allure red. In Fig. 5C, MIES exhibited high selectivity for imprinting molecule amaranth compared with the analogs erythrosine, new coccine and allure red, while the controlled NIES showed low binding values for all of them.

3.5. Reproducibility and stability

Five batches of MIES were investigated to compare their ΔI_p before and after adsorption in 1 μmol L^{-1} amaranth PBS and the RSD was 4.7%, confirming that the preparation method was highly reproducible. The reproducibility of the imprinted sensor was estimated by comparing ΔI_p at room temperature after successive ten times tests with the same electrode. RSD of 2.5% was obtained which indicated good reproducibility. The MIES retained a response of 94% of peak current value after one week stored at 4 °C and decreased by about 10% after two weeks. And there was

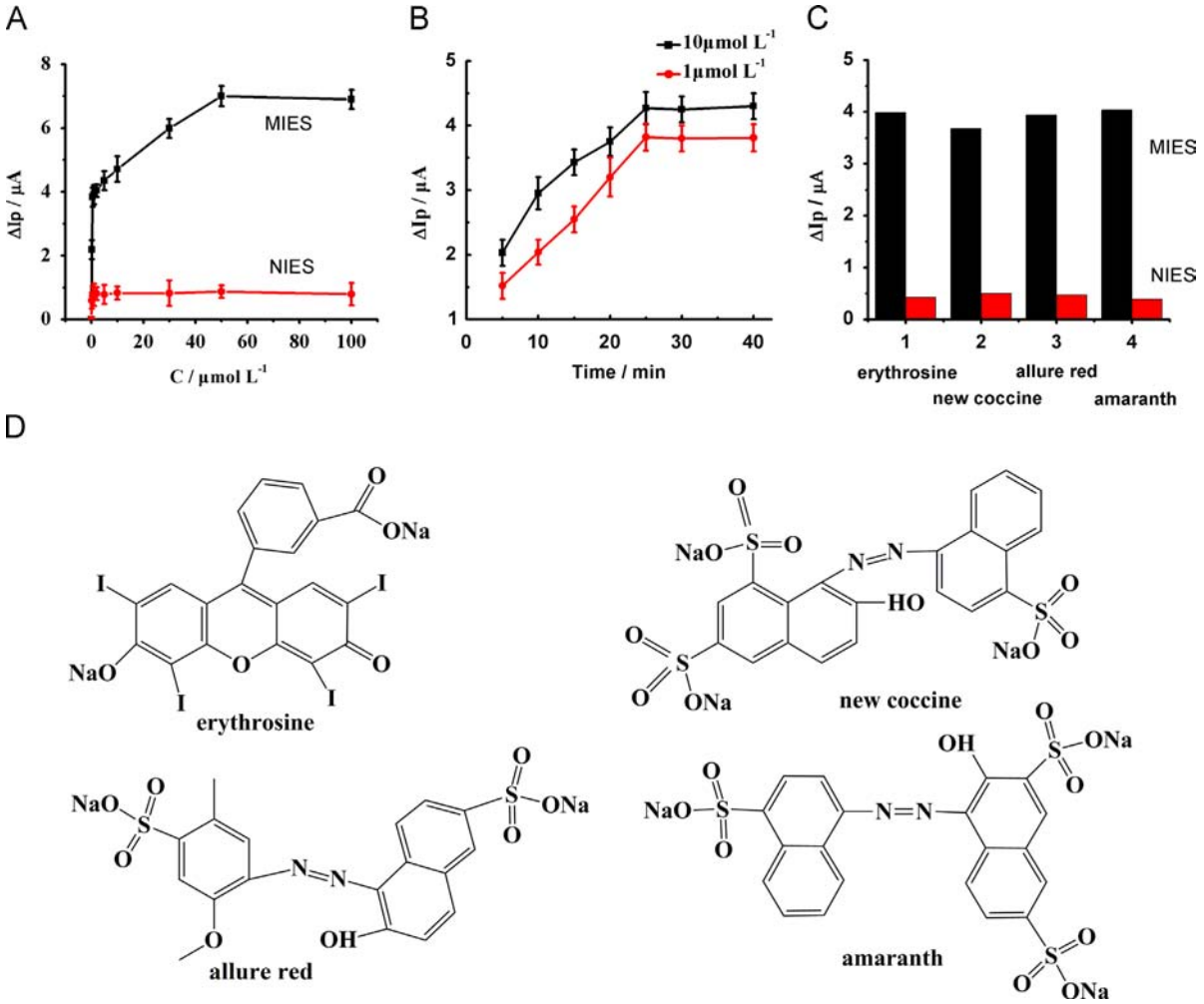

Fig. 5. (A) the adsorption isotherms of MIES and NIES, (B) adsorption kinetics of MIES, (C) the changed DPV response of MIES and NIES before and after adsorption to 1 μmol L^{-1} amaranth solution (d), mixture of 1 μmol L^{-1} amaranth and 100-fold molar concentration ratio of erythrosine (a), allure red (b) and new coccine (c), and (D) molecular structures of erythrosine, new coccine, allure red and amaranth.

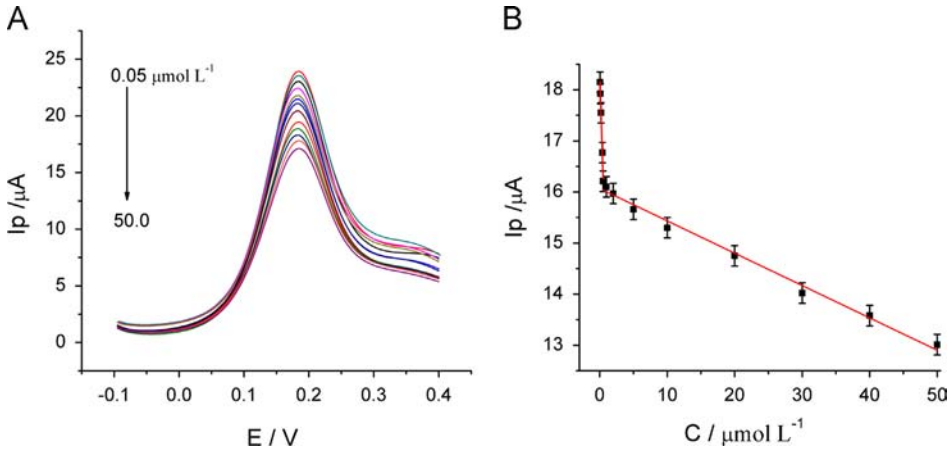

Fig. 6. (A) DPV curves of increasing amaranth concentration in 1 mmol L^{-1} of $K_3[Fe(CN)_6]$ and 0.1 mol L^{-1} of KCl, and (B) the linear relationship of I_p and the concentrations of amaranth ($n=3$).

Table 1
Results of detection of amaranth in different fruit drinks.

Fruit drinks	Content (μg mL^{-1})	Spiked amount (μg mL^{-1})	Found level (μg mL^{-1})	Recovery (%)	RSD (%)
Grapes flavor	12.76	10.21	21.49	93.56	2.69
		12.76	25.11	98.40	2.13
		15.31	27.07	100.81	1.91
Watermelon flavor	8.65	7.00	15.65	93.15	2.51
		8.75	17.4	97.73	1.98
		10.25	18.9	94.36	2.03
Peach flavor	9.00	7.25	16.25	94.24	2.34
		9.00	18.00	96.78	2.56
		10.75	19.75	98.27	2.97

Table 2
Comparison of some electrodes for the detection of amaranth.

Electrodes	Detection potential (V)	Signal molecule	Detection limit (nM)	Linear range	References
Hanging mercury drop electrode	About −0.45	Amaranth	50	50–266 nM	[49]
Al_2O_3-microfibers-modified CPE	About 0.72	Amaranth	0.75	1–150 nM	[50]
CNTs-modified GCE	About 0.72	Amaranth	35	40–800 nM	[51]
The doped imprinted layers modified MGCE	About 0.18	$K_3[Fe(CN)_6]$	50	0.05–50 μM	

no obvious change in the oxidation potential and profile of the peak.

3.6. Quantitative detection of amaranth and sample analysis

DPV was investigated to evaluate the performance of the fabricated MIES under optimized conditions. The current signal was directly related to the amount of amaranth captured on the surface of imprinted electrode. Fig. 6A displays DPV detection of amaranth with the presence of $[Fe(CN)_6]^{3-/4-}$ couple. The amount of amaranth captured on MIES increased gradually with the increasing concentrations, resulting in the enhancement for hindering the redox probe and the decrease response of peak current. Fig. 6B shows the linear relationship between the concentration of amaranth and current value of oxidation peak. The achieved linear regression equation were I_p (μA) = −4.22 C (μmol L^{-1}) + 18.37 (Er ± 0.17) in the range of 0.05–0.50 μmol L^{-1} and I_p (μA) = −0.06 C (μmol L^{-1}) + 16.04 (Er ± 0.19) in the range of 0.50–50.0 μmol L^{-1} with correlation coefficient of 0.993 and 0.988, respectively.

The as-proposed MIES was used for the determination of amaranth in fruit drinks. The content and recoveries of amaranth are listed in Table 1. As can be seen, the recoveries were in the range of 93.15–100.81% with the RSD < 3.0%. Moreover, the comparison of some electrodes for the detection of amaranth is shown in Table 2. The linear range by the MIES was wider due to the use of redox probe $K_3[Fe(CN)_6]$, which avoided the interferences of oxidation products and analogs.

3.7. Interference

The potential interferences for the determination of amaranth were studied. Under the optimized conditions, the oxidation peak current of redox probe $K_3[Fe(CN)_6]$ by DPV was measured in the presence of different concentrations of interferents, and the change of peak current value was then checked. No influence on the detection of 0.1 μmol L^{-1} amaranth was found after the addition of 1000-fold concentrations of glucose, sucrose, citric acid, K^+, Na^+; 100-food concentrations of erythrosine, new coccine and allure red (The peak current change is below 5%).

4. Conclusions

A novel MIES based on magnetic field induced self-assembly and electropolymerization was fabricated and studied for the determination of the azo dye amaranth. The Fe_3O_4@rGO composites synthesized by a facile method using hydrazine as reducer could be fast oriented and assembled on the surface of MGCE by magnetic field induction. The thickness of the doped imprinted sensing membrane could be easily controlled by changing the concentration of Fe_3O_4@rGO composites. The fabricated MIES with the help of MDSA exhibited good sensitivity, selectivity, reproducibility and efficiency for the determination of amaranth in fruit drinks.

For the exploration of Fe_3O_4@rGO composites and MDSA in the preparation of MIPs, an interesting assembling approach was exhibited for the fabrication of electrochemical and biological sensing membrane. The external magnetic field employed for modified electrodes exhibited some merits: fast orientation and immobilization of the magnetic composites, easy formation of nanostructure film avoiding serious aggregation, convenient modulation of thickness and morphology of modified film.

However, in the study, we only used the external magnetic field under fixed magnetic field strength in the exploration of the thickness and morphologies of the doped imprinted sensing membrane. Different magnetic field strength should be employed for obtaining more details and regularities while discussing the structures and physical and electrochemical performances of the doped MIPs or modified electrodes. And further researches have been carried out.

Acknowledgment

This work was supported by National Natural Science Foundation of China (Nos. 81273480 and 21175070).

Appendix A. Supporting information

Supplementary data associated with this article can be found in the online version at http://dx.doi.org/10.1016/j.talanta.2014.01.060.

References

[1] Z. Wang, X. Zhou, J. Zhang, F. Boey, H. Zhang, J. Phys. Chem. C 32 (2009) 14071.
[2] I. Baravik, R. Tel-Vered, O. Ovits, I. Willner, Langmuir 24 (2009) 13978.
[3] H. Lalo, Y. Bon-Saint-Côme, B. Plano, M. Etienne, A. Walcarius, A. Kuhn, Langmuir 5 (2012) 2323.
[4] W. Liao, T. Chou, Anal. Chem. 12 (2006) 4219.
[5] J.W. Jo, J.W. Jung, J.U. Lee, W.H. Jo, ACS Nano 9 (2010) 5382.
[6] A.S. Kumar, P. Swetha, Colloids Surf. A Physicochem. Eng. Asp. 1–3 (2011) 597.
[7] C. Lee, S. Wang, C. Yuan, M. Wen, K. Chang, Biosens. Bioelectron. 6 (2007) 877.
[8] J. Tian, L. Yuan, M. Zhang, F. Zheng, Q. Xiong, H. Zhao, Langmuir 25 (2012) 9365.
[9] M. Grzelczak, J. Vermant, E.M. Furst, L.M. Liz-Marzán, ACS Nano 7 (2010) 3591.
[10] T. Salditt, U.S. Schubert, Rev. Mol. Biotechnol. 1 (2002) 55.
[11] E. Akyilmaz, M. Turemis, Electrochim. Acta 18 (2010) 5195.
[12] Y. Zhang, C. Ji, Anal. Chem. 12 (2010) 5275.
[13] X. Zhou, X. Zheng, R. Lv, D. Kong, Q. Li, Electrochim. Acta (2013) 164.
[14] J. Li, H. Xie, L. Chen, Sens. Actuators B Chem. 1 (2011) 239.
[15] X. Feng, F. Ruan, R. Hong, J. Ye, J. Hu, G. Hu, Z. Yang, Langmuir 6 (2011) 2204.
[16] M.V. Walter, N. Cheval, O. Liszka, M. Malkoch, A. Fahmi, Langmuir 14 (2012) 5947.
[17] M. Asbahi, K.T.P. Lim, F. Wang, H. Duan, N. Thiyagarajah, V. Ng, J.K.W. Yang, Langmuir 49 (2012) 16782.
[18] P. Kumar, Nanoscale Res. Lett. 9 (2010) 1367.
[19] Q. Tang, J. Wu, X. Sun, Q. Li, J. Lin, J. Colloid Interface Sci. 1 (2009) 155.
[20] Z. Xu, C. Hu, H. Guoxin, Thin Solid Films 13 (2011) 4324.
[21] W. Li, R. Xu, L. Zheng, J. Du, Y. Zhu, R. Huang, H. Deng, Carbohydr. Polym. 4 (2012) 1656.
[22] M. Yin, J. Qian, Q. An, Q. Zhao, Z. Gui, J. Li, J. Membr. Sci. 1–2 (2010) 43.
[23] S. Liu, J. Yan, G. He, D. Zhong, J. Chen, L. Shi, X. Zhou, H. Jiang, J. Electroanal. Chem. (2012) 40.
[24] M. Motornov, S.Z. Malynych, D.S. Pippalla, B. Zdyrko, H. Royter, Y. Roiter, M. Kahabka, A. Tokarev, I. Tokarev, E. Zhulina, K.G. Kornev, I. Luzinov, S. Minko, Nano Lett. 7 (2012) 3814.
[25] B. Dong, T. Zhou, H. Zhang, C.Y. Li, ACS Nano 6 (2013) 5192.
[26] R. Olivé-Monllau, F.X. Muñoz-Pascual, E. Baldrich, Sens. Actuators B Chem. (2013) 685.
[27] L. Xu, J. Du, Y. Deng, N. He, Electrochem. Commun. 10 (2010) 1329.
[28] F. Li, L. Mei, Y. Li, K. Zhao, H. Chen, P. Wu, Y. Hu, S. Cao, Biosens. Bioelectron. 10 (2011) 4253.
[29] S. Pan, Y. Zhang, H. Shen, M. Hu, Chem. Eng. J. (2012) 564.
[30] L. Peng, P. Qin, M. Lei, Q. Zeng, H. Song, J. Yang, J. Shao, B. Liao, J. Gu, J. Hazard. Mater. (2012) 193.
[31] H. Zhang, Y. Shi, Anal. Chim. Acta (2012) 54.
[32] J. Qiu, M. Xiong, R. Liang, H. Peng, F. Liu, Biosens. Bioelectron. 8 (2009) 2649.
[33] B.H. Nguyen, L.D. Tran, Q.P. Do, H.L. Nguyen, N.H. Tran, P.X. Nguyen, Mater. Sci. Eng. C 4 (2013) 2229.
[34] K.S. Novoselov, A.K. Geim, S.V. Morozov, D. Jiang, Y. Zhang, S.V. Dubonos, I.V. Grigorieva, A.A. Firsov, Science (2004).
[35] B. Zhang, L. Fan, H. Zhong, Y. Liu, S. Chen, J. Am. Chem. Soc. 27 (2013) 10073.
[36] A. Le Goff, B. Reuillard, S. Cosnier, Langmuir 27 (2013) 8736.
[37] X. Liu, H. Zhu, X. Yang, Talanta (2011) 243.
[38] H. Yin, Y. Zhou, Q. Ma, S. Ai, Q. Chen, L. Zhu, Talanta 4 (2010) 1193.
[39] Y. Li, T. Wen, C. Xue, Q. Han, Y. Wang, J. Hong, X. Zhou, H. Jiang, Biosens. Bioelectron. (2013) 287.
[40] T. Wen, C. Xue, Y. Li, Y. Wang, R. Wang, J. Hong, X. Zhou, H. Jiang, J. Electroanal. Chem. (2012) 121.
[41] C. Xue, Q. Han, Y. Wang, J. Wu, T. Wen, R. Wang, J. Hong, X. Zhou, H. Jiang, Biosens. Bioelectron. (2013) 199.
[42] R. Sarıkaya, M. Selvi, F. Erkoç, Chemosphere 8 (2012) 974.
[43] P. Mpountoukas, A. Pantazaki, E. Kostareli, P. Christodoulou, D. Kareli, S. Poliliou, C. Mourelatos, V. Lambropoulou, T. Lialiaris, Food Chem. Toxicol. 10 (2010) 2934.
[44] Y. Yao, S. Miao, S. Liu, L.P. Ma, H. Sun, S. Wang, Chem. Eng. J. (2012) 326.
[45] J. Wang, B. Tang, T. Tsuzuki, Q. Liu, X. Hou, L. Sun, Chem. Eng. J. (2012) 258.
[46] J. Guo, S. Zhu, Z. Chen, Y. Li, Z. Yu, Q. Liu, J. Li, C. Feng, D. Zhang, Ultrason. Sonochem. 5 (2011) 1082.
[47] S. Zhu, J. Guo, J. Dong, Z. Cui, T. Lu, C. Zhu, D. Zhang, J. Ma, Ultrason. Sonochem. 3 (2013) 872.
[48] J. Guo, R. Wang, W.W. Tjiu, J. Pan, T. Liu, J. Hazard. Mater. (2012) 63.
[49] Y. Ni, J. Bai, Talanta 1 (1997) 105.
[50] Y. Zhang, T. Gan, C. Wan, K. Wu, Anal. Chim. Acta (2013) 53.
[51] P. Wang, X. Hu, Q. Cheng, X. Zhao, X. Fu, K. Wu, J. Agric. Food Chem. 23 (2010) 12112.